Chapter 2

Space-Time Transmit-Receive Design for Colocated MIMO Radar

Guolong Cui, Xianxiang Yu and Lingjiang Kong

Additional information is available at the end of the chapter

http://dx.doi.org/10.5772/intechopen.71946

Abstract

This chapter deals with the design of multiple input multiple-output (MIMO) radar space-time transmit code (STTC) and space-time receive filter (STRF) to enhance moving targets detection in the presence of signal-dependent interferences, where we assume that some knowledge of target and clutter statistics are available for MIMO radar system according to a cognitive paradigm by using a site-specific (possible dynamic) environment database. Thus, an iterative sequential optimization algorithm with ensuring the convergence is proposed to maximize the signal to interference plus noise ratio (SINR) under the similarity and constant modulus constraints on the probing waveform. In particular, each iteration of the proposed algorithm requires to solve the hidden convex problems. The computational complexity is linear with the number of iterations and polynomial with the sizes of the STTW and the STRF. Finally, the gain and the computation time of the proposed algorithm also compared with the available methods are evaluated.

Keywords: multiple input multiple output (MIMO), space-time transmit code (STTC), space-time receive filter (STRF), signal-dependent interferences, signal to interference plus noise ratio (SINR)

1. Introduction

Multiple-input multiple-output (MIMO) radar emits multiple probing signals via its transmit antennas, which provides the greater flexibility for the design of the whole radar system, and boosts the development of more sophisticated signal processing algorithms [1]. On the basis of the configurations of transmitter/receiver antennas, MIMO radar systems can be classified into two categories: widely distributed [2, 3] and colocated [4, 5]. The former has different angles of view on the target owing to widely separated antennas, and this feature can be used to improve the performance of target detection and angle estimation, as well as the capabilities of target

identification and classification [6]. The latter shares the same aspect angle of the target by using tightly spaced antennas. However, colocated MIMO radar exploits the waveform diversity to form a long virtual array, thus providing better results concerning spatial resolution, target localization, and the interference rejection, as well as obtaining the degrees of freedom for the design of transmit beam pattern [1, 7, 8].

Recently, colocated MIMO radar waveform design is a hot and challenging topic and has received significant attention. In general, these works can be divided into two categories. The first category focuses on the fast-time waveforms design exploiting some a priori information. In particular, in [6], by using the a priori knowledge of target power spectral density, the minimax robust waveforms are designed based on the rules of the mutual information (MI) and minimum mean-square error (MMSE). In [9], MIMO waveforms for the case of an extended target are devised based on the maximization of signal-to-interference plus-noise ratio (SINR) through a gradient-based algorithm assuming the knowledge of both the target and signal-dependent clutter statistics. In [10], by considering MMSE as figure of merit, MIMO radar waveforms are synthesized under signal-dependent clutter. The join design of the transmit waveform and the receive filter is addressed for improving the extended target delectability in the presence of signal-dependent clutter, by employing a cycle iteration algorithm with ensuring convergence [11]. In [12], by designing the transmit waveform and the receive filter, two sequential optimization algorithms are proposed to maximize SINR subject to the constant modulus and similarity constraints. Based on the rule of the worst-case output SINR in the presence of unknown target angle, the robust joint design of transmit waveform and the receive filter is considered [13]. Some more works can be found in [7, 8, 14, 15].

The second category addresses the MIMO radar space-(slow) time code design for moving target scenarios. In particular, in [16], MIMO radar slow-time code shares the ability of improving the resolution in angle-Doppler images and obtaining enhanced moving target detection performance. In [17], the signal-dependent interference is alleviated by the space-time coding framework based on a beamspace space-time adaptive processing (STAP). In [18], based on the max-min SINR optimization criteria, the time-division beamforming signal is designed for a multiple target scenario. For a moving point-like target detection, based on the worst case SINR over the actual and signal-dependent clutter statistics, the robust joint design of the space-time transmit code (STTC) satisfying the energy and similarity constraints and the space-time receive filter (STRF) is addressed in [19].

This chapter handles the joint design of the STTC and STRF with the aim of enhancing the moving target detectability under signal-dependent interferences and white Gaussian noise. Unlike [19, 20], some knowledge of target and clutter statistics is assumed to be available. In particular, the SINR is considered as figure of merit to maximize subject to a constant modulus constraint on the transmit signal in addition to a similarity constraint. To deal with the resulting nonconvex design problem, an iterative algorithm ensuring convergence is proposed. Each iteration of the proposed algorithm involves the solution of hidden convex problems. Specifically, both a convex problem with closed-form solution and a set of fractional programming problems, which can be globally solved through the Dinkelback's algorithm, are solved. The resulting computational complexity is linear with the number of iterations and polynomial with the sizes of the STTC and the STRF.

The remainder of the chapter is organized as follows. In Section 2, the system model is formalized. In Section 3, the constrained optimization problem under constant modulus and similarity constraints is formulated. In Section 4, the new optimization algorithm is presented. In Section 5, the performance of the new procedure is evaluated. Finally, in Section 6, concluding remarks and possible future research tracks are provided.

2. System model

We focus on a colocated narrow band MIMO radar system consisting of N_T transmitters antennas and N_R receivers. Each transmitter emits a slow-time phase-coded coherent train with K pulses. Let $s(k) = [s_1(k), s_2(k), \cdots, s_{N_T}(k)]^T \in \mathbb{C}^{N_T}$, $k = 1, 2, \cdots, K$ denote the transmitted space code vector at the kth transmission interval, where $s_{n_t}(k)$ denotes the kth transmitted phase-code pulse of the n_tth transmitting antenna, for $n_t = 1, 2, \cdots, N_T$, $(\cdot)^T$ stands for the transpose, and $\mathbb{C}^N$ is the set of N-dimensional vectors of complex numbers. At each receiver, the received waveform is downconverted to baseband, undergoes a pulse matched filtering operation, and then is sampled. Hence, the observations of the kth slow-time sample for a far-field moving target at the azimuth angle θ_0 can be expressed as [21]

$$x(k) = \alpha_0 e^{j2\pi(k-1)v_{d_0}} \mathbf{A}(\theta_0)\, s(k) + d(k) + v(k), \tag{1}$$

where

- α_0 is a complex parameter taking into account the target radar cross section (RCS), channel propagation effects, and other terms involved into the radar range equation.
- v_{d_0} denotes the normalized target Doppler frequency, which is related to the radial velocity v_r via the equation $v_{d_0} = 2v_r T/\lambda$ with λ being the carrier wavelength and T being the pulse repetition time (PRT).
- $\mathbf{A}(\theta) = a_r^*(\theta) a_t{}^\dagger(\theta)$, in which $a_t(\theta)$ and $a_r(\theta)$ denote the transmit spatial steering vector and the receive spatial steering vector at the azimuth angle θ, respectively, and $(\cdot)^*$ and $(\cdot)^\dagger$ are the conjugate and the conjugate transpose operators, respectively. In particular, for the uniform linear arrays (ULAs), they are given by

$$a_t(\theta) = \frac{1}{\sqrt{N_T}} \left[1, e^{j2\pi \frac{d_T}{\lambda} \sin\theta}, \cdots, e^{j2\pi \frac{d_T}{\lambda}(N_T-1)\sin\theta}\right]^T, \tag{2}$$

$$a_r(\theta) = \frac{1}{\sqrt{N_R}} \left[1, e^{j2\pi \frac{d_R}{\lambda} \sin\theta}, \cdots, e^{j2\pi \frac{d_R}{\lambda}(N_R-1)\sin\theta}\right]^T \tag{3}$$

with d_T and d_R being the array interelement spacing of the transmitter and the receiver, respectively.

- $d(k) \in \mathbb{C}^{N_R}$, $k = 1, 2, \cdots, K$, considering M signal-dependent uncorrelated point-like interfering scatterers. Specifically, as shown in **Figure 1**, the angle space is discretized as $\Theta = \{0, 1, \cdots, L\} \times \frac{2\pi}{(L+1)}$. For the mth interfering source located at the range-azimuth bin

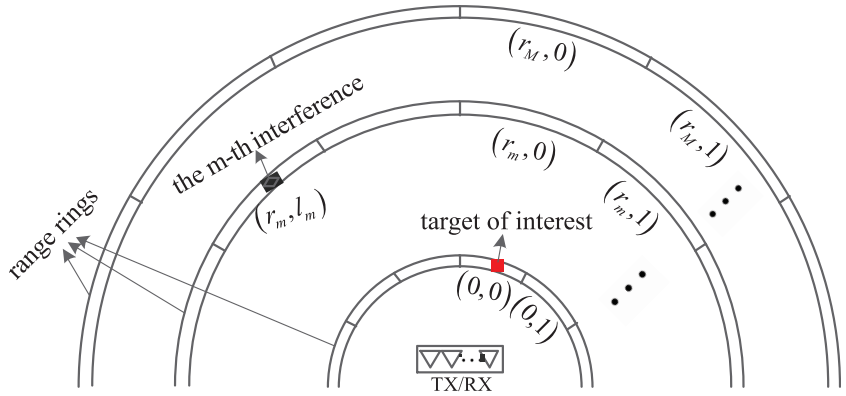

Figure 1. Range-azimuth bins (the target of interest is represented by the red (solid) circle).

$(\boldsymbol{r_m}, \boldsymbol{l_m})$, $\boldsymbol{r_m} \in \{\mathbf{0}, \mathbf{1}, \cdots, \boldsymbol{K}-\mathbf{1}\}$, $\boldsymbol{l_m} \in \{\mathbf{0}, \mathbf{1}, \cdots, \boldsymbol{L}\}$, the received interfering vector $\boldsymbol{d}(\boldsymbol{k})$ can be expressed as the superposition of the returns from $\boldsymbol{M}$ interference sources, i.e.,

$$\boldsymbol{d}(\boldsymbol{k}) = \sum_{\boldsymbol{m}=\mathbf{1}}^{\boldsymbol{M}} \boldsymbol{\rho_m} e^{j2\pi v_{d_m}(k-1)} \mathbf{A}(\boldsymbol{\theta_m})\, \boldsymbol{s}(\boldsymbol{k}-\boldsymbol{r_m}), \mathbf{0} \le \boldsymbol{r_m} \le \boldsymbol{k}-\mathbf{1}, \tag{4}$$

with $\boldsymbol{\rho_m}$, v_{d_m}, and $\boldsymbol{\theta_m}$, respectively, the complex amplitude, the normalized Doppler frequency, and the look angle, given by $\boldsymbol{\theta_m} = \frac{2\pi}{(L+1)} \boldsymbol{l_m}$ of the $\boldsymbol{m}$th interferences. Furthermore, $\boldsymbol{M}$ is nominally equal to $\boldsymbol{K} \times (\boldsymbol{L}+\mathbf{1})$.

- $\boldsymbol{v}(\boldsymbol{k}) \in \mathbb{C}^{N_R}$, $\boldsymbol{k} = \mathbf{1}, \mathbf{2}, \cdots, \boldsymbol{K}$ denotes additive noise, modeled as independent and identically distributed (i.i.d.) complex circular zero-mean Gaussian random vector, i.e., $\boldsymbol{v}(\boldsymbol{k}) \sim \mathcal{CN}(\mathbf{0}, \sigma^2 \boldsymbol{I}_{N_R})$, where $\boldsymbol{I}_{N_R}$ denotes $\boldsymbol{N_R} \times \boldsymbol{N_R}$-dimensional identity matrix.

Let $\boldsymbol{x} = \left[\boldsymbol{x}^T(\mathbf{1}), \cdots, \boldsymbol{x}^T(\boldsymbol{K})\right]^T$, $\boldsymbol{s} = \left[\boldsymbol{s}^T(\mathbf{1}), \cdots, \boldsymbol{s}^T(\boldsymbol{K})\right]^T$, $\boldsymbol{d} = \left[\boldsymbol{d}^T(\mathbf{1}), \cdots, \boldsymbol{d}^T(\boldsymbol{K})\right]^T$, and $\boldsymbol{v} = \left[\boldsymbol{v}^T(\mathbf{1}), \cdots, \boldsymbol{v}^T(\boldsymbol{K})\right]^T$. Then, Eq. (1) can be expressed in a compact form as

$$\boldsymbol{x} = \boldsymbol{\alpha_0} \widehat{\mathbf{A}}\left(v_{d_0}, \boldsymbol{\theta_0}\right) \boldsymbol{s} + \boldsymbol{d} + \boldsymbol{v}, \tag{5}$$

where

$$\widehat{\mathbf{A}}(v_d, \boldsymbol{\theta_0}) = \mathbf{Diag}(\boldsymbol{p}(v_d)) \otimes \mathbf{A}(\boldsymbol{\theta_0}) \tag{6}$$

with $\boldsymbol{p}(v_d) = \left[\mathbf{1}, e^{j2\pi v_d}, \cdots, e^{j2\pi(K-1)v_d}\right]^T$ being the temporal steering vector, $\otimes$ denotes the Kronecker product, and $\mathbf{Diag}(\cdot)$ denotes the diagonal matrix formed by the entries of the vector argument. Additionally, we assume that the noise vector $\boldsymbol{v}$ is a zero-mean circular complex Gaussian random vector with covariance matrix $\boldsymbol{\Sigma_v} = \mathbb{E}\left[\boldsymbol{v}\, \boldsymbol{v}^\dagger\right] = \sigma_v^2 \boldsymbol{I}_{N_R K}$. Finally, interference vector $\boldsymbol{d}$ can be expressed as

$$\boldsymbol{d} = \sum_{m=1}^{M} \boldsymbol{\rho}_m \mathbf{P}_{r_m} \widehat{\mathbf{A}}\left(v_{d_m}, \boldsymbol{\theta}_m\right) \boldsymbol{s}, \tag{7}$$

where $\mathbf{P}_{r_m}$ is given by

$$\mathbf{P}_{r_m} = \mathbf{J}^{r_m} \otimes \mathbf{I}_{N_R}, \tag{8}$$

in which $\mathbf{J}^r$ denotes the shift matrix [23], whose $(\boldsymbol{k_1}, \boldsymbol{k_2})$th entry is defined as[1],

$$\mathbf{J}^r(k_1, k_2) = \begin{cases} \mathbf{1} & k_1 - k_2 = r \\ \mathbf{0} & k_1 - k_2 \neq r, \end{cases} \tag{9}$$

$\boldsymbol{r} \in \{\mathbf{0}, \mathbf{1}, \cdots, \boldsymbol{K}-\mathbf{1}\}$ and $(\boldsymbol{k_1}, \boldsymbol{k_2}) \in \{\mathbf{1}, \mathbf{2}, \cdots, \boldsymbol{K}\}^{\mathbf{2}}$. In particular, we assume that $\boldsymbol{\rho}_m$, $\boldsymbol{m} = \mathbf{1}, \mathbf{2}, \cdots, \boldsymbol{M}$, and $\boldsymbol{\alpha_0}$ are a zero-mean uncorrelated random variables with, respectively, $\sigma_m^2 = \mathbb{E}\left[|\boldsymbol{\rho}_m^2|\right]$ and $\sigma_0^2 = \mathbb{E}\left[|\boldsymbol{\alpha_0}|^2\right]$. As to the normalized Doppler frequency of the interfering signals, we model v_{d_m} as a random variable uniformly distributed around a mean Doppler frequency $\overline{v}_{d_m}$, i.e.,

$$v_{d_m} \sim \boldsymbol{U}\left(\overline{v}_{d_m} - \frac{\boldsymbol{\varepsilon}_m}{\mathbf{2}}, \overline{v}_{d_m} + \frac{\boldsymbol{\varepsilon}_m}{\mathbf{2}}\right), \boldsymbol{m} \in \mathbf{1}, \mathbf{2}, \cdots, \boldsymbol{M} \tag{10}$$

where $\boldsymbol{\varepsilon}_m$ accounts for the uncertainty on v_{d_m}. Basing on the previous assumptions, the interference vector $\boldsymbol{d}$ has zero mean and covariance matrix

$$\boldsymbol{\Sigma}_d(\boldsymbol{s}) \quad = \mathbb{E}\left[\boldsymbol{d}\boldsymbol{d}^{\boldsymbol{\dagger}}\right] = \sum_{m=1}^{M} \left(\mathbf{J}^{r_m} \otimes \mathbf{A}(\boldsymbol{\theta}_m)\right) \left[\left(\boldsymbol{s}\boldsymbol{s}^{\boldsymbol{\dagger}}\right) \odot \boldsymbol{\Xi}_m\right] \left(\mathbf{J}^{r_m} \otimes \mathbf{A}(\boldsymbol{\theta}_m)\right)^{\boldsymbol{\dagger}}, \tag{11}$$

where

$$\boldsymbol{\Xi}_m = \sigma_m^2 \boldsymbol{\Phi}_{\boldsymbol{\varepsilon}_m}^{\overline{v}_{d_m}} \otimes \boldsymbol{\Upsilon}_t, \tag{12}$$

in which

$$\boldsymbol{\Phi}_{\boldsymbol{\varepsilon}_m}^{\overline{v}_{d_m}}(k_1, k_2) = e^{j2\pi\overline{v}_{d_m}(k_1 - k_2)} \frac{\sin\left[\pi\boldsymbol{\varepsilon}_m(k_1 - k_2)\right]}{\pi\boldsymbol{\varepsilon}_m(k_1 - k_2)}, \forall (\boldsymbol{k_1}, \boldsymbol{k_2}) \in \{\mathbf{1}, \mathbf{2}, \cdots, \boldsymbol{K}\}^{\mathbf{2}}, \tag{13}$$

and $\boldsymbol{\Upsilon}_t = \mathbf{1}_t \mathbf{1}_t{}^T$ with $\mathbf{1_t} = [\mathbf{1}, \mathbf{1}, \cdots, \mathbf{1}]^T$ being the $\boldsymbol{N_T} \times \mathbf{1}$ vector, $\odot$ and $\mathbb{E}[\cdot]$ denote the Hadamard product and the statistical expectation, respectively. This expression, for the covariance matrix $\boldsymbol{\Sigma}_d(\boldsymbol{s})$, follows from the results obtained in ([19], Appendix 1).

Inspection of (11) and (12) reveals that the interference covariance matrix $\boldsymbol{\Sigma}_d(\boldsymbol{s})$ requires the knowledge of $\boldsymbol{\theta}_m$ and σ_m^2 as well as $\overline{v}_{d_m}$ and $\boldsymbol{\varepsilon}_m$, for $\boldsymbol{m} = \mathbf{1}, \mathbf{2}, \cdots, \boldsymbol{M}$. These information can be obtained according to a cognitive paradigm [22–24] through exploiting a site-specific (possible dynamic) environment database, which involves a geographical information system (GIS),

[1] Notice that based on its definition, the shift matrix satisfies the condition $\mathbf{J}^r = \mathbf{J}^{-rT}$.

digital terrain maps, previous scans, tracking files, clutter models (in terms of electromagnetic reflectivity and spectral density), and meteorological information.

3. Problem formulation

This section formulates the joint design problem of the STTC and STRF based on the maximization of the output SINR considering practical constraints.

3.1. Output SINR

Letting the observations $\boldsymbol{x}$ be processed via the STRF $\boldsymbol{w} \in \mathbb{C}^{N_R K}$, the SINR $\widehat{\boldsymbol{\rho}}(\boldsymbol{s}, \boldsymbol{w})$ at the output of the receiver can be expressed as

$$\widehat{\boldsymbol{\rho}}(\boldsymbol{s}, \boldsymbol{w}) = \frac{\left|\boldsymbol{\alpha}_0 \boldsymbol{w}^{\dagger} \widehat{\mathbf{A}}\left(v_{d_0}, \boldsymbol{\theta}_0\right) \boldsymbol{s}\right|^2}{\mathbb{E}\left[\left|\boldsymbol{w}^{\dagger} \boldsymbol{d}\right|^2\right] + \mathbb{E}\left[\left|\boldsymbol{w}^{\dagger} \boldsymbol{v}\right|^2\right]} = \frac{\sigma_0^2 \boldsymbol{w}^{\dagger} \widehat{\mathbf{A}}\left(v_{d_0}, \boldsymbol{\theta}_0\right) \boldsymbol{s} \boldsymbol{s}^{\dagger} \widehat{\mathbf{A}}^{\dagger}\left(v_{d_0}, \boldsymbol{\theta}_0\right) \boldsymbol{w}}{\boldsymbol{w}^{\dagger} \boldsymbol{\Sigma}_d(\boldsymbol{s}) \boldsymbol{w} + \sigma_v^2 \boldsymbol{w}^{\dagger} \boldsymbol{w}}, \tag{14}$$

where we exploit

$$\mathbb{E}\left[\left|\boldsymbol{w}^{\dagger} \boldsymbol{d}\right|^2\right] = \boldsymbol{w}^{\dagger} \mathbb{E}\left[\boldsymbol{d} \boldsymbol{d}^{\dagger}\right] \boldsymbol{w} \tag{15}$$

and

$$\mathbb{E}\left[\left|\boldsymbol{w}^{\dagger} \boldsymbol{v}\right|^2\right] = \boldsymbol{w}^{\dagger} \mathbb{E}\left[\boldsymbol{v}\, \boldsymbol{v}^{\dagger}\right] \boldsymbol{w} \tag{16}$$

and assume $\boldsymbol{w} \neq \mathbf{0}$ and the independence between the disturbance and the noise random processes.

In particular, the numerator in (14) denotes the useful energy at the output of the STRF, $\boldsymbol{w}^{\dagger} \boldsymbol{\Sigma}_d(\boldsymbol{s}) \boldsymbol{w}$ and $\sigma_v^2 \boldsymbol{w}^{\dagger} \boldsymbol{w}$ represent the clutter energy and noise energy, respectively, at the output of $\boldsymbol{w}$. Observe that the clutter energy $\boldsymbol{w}^{\dagger} \boldsymbol{\Sigma}_d(\boldsymbol{s}) \boldsymbol{w}$ functionally relies on the STTC $\boldsymbol{w}$ and the STRF $\boldsymbol{s}$ through $\boldsymbol{\Sigma}_d(\boldsymbol{s})$ as well as the useful energy. Furthermore, we note that the objective function $\widehat{\boldsymbol{\rho}}(\boldsymbol{s}, \boldsymbol{w})$ requires that the exact angle $\boldsymbol{\theta}_0$ and normalized Doppler frequency v_{d_0} are known. However, from a practical point of view, the explicit knowledge of $\boldsymbol{\theta}_0$ and v_{d_0} cannot be available. To circumvent this drawback, the averaged SINR defined as $\boldsymbol{\rho}(\boldsymbol{s}, \boldsymbol{w}) = \mathbb{E}[\widehat{\boldsymbol{\rho}}(\boldsymbol{s}, \boldsymbol{w})]$ as figure of merit is exploited. More specifically, we suppose that v_{d_0} and $\boldsymbol{\theta}_0$ are independent random variables uniformly distributed around a mean Doppler frequency $\overline{v}_{d_0}$ and a mean azimuth $\overline{\boldsymbol{\theta}}_0$, respectively, i.e., $v_{d_0} \sim \boldsymbol{U}\left(\overline{v}_{d_0} - \frac{\varepsilon_0}{2}, \overline{v}_{d_0} + \frac{\varepsilon_0}{2}\right)$, $\boldsymbol{\theta}_0 \sim \boldsymbol{U}\left(\overline{\boldsymbol{\theta}}_0 - \frac{\vartheta_0}{2}, \overline{\boldsymbol{\theta}}_0 + \frac{\vartheta_0}{2}\right)$, where $\sim$ means "*distribute*" and $\boldsymbol{U}$ represents uniform distribution and $\boldsymbol{\varepsilon}_0$ and $\boldsymbol{\vartheta}_0$ accounts for the uncertainty on v_{d_0} and $\boldsymbol{\theta}_0$, respectively. Interestingly, after some algebraic manipulations, the objective function $\boldsymbol{\rho}(\boldsymbol{s}, \boldsymbol{w})$ shares the following two equivalent expressions,

where

$$\boldsymbol{\Gamma}(\boldsymbol{S}) = \sigma_0^2 \mathbb{E}\Big[(\mathbf{Diag}(\boldsymbol{p}(v_d)) \otimes \mathbf{A}(\boldsymbol{\theta}_0)) \boldsymbol{S} \Big((\mathbf{Diag}(\boldsymbol{p}(v_d)))^{\dagger} \otimes \mathbf{A}^{\dagger}(\boldsymbol{\theta}_0)\Big)\Big] \tag{17}$$

$$\boldsymbol{\Sigma}_{dv}(\boldsymbol{S}) = \sum_{m=1}^{M} (\mathbf{J}^{r_m} \otimes \mathbf{A}(\boldsymbol{\theta}_m))(\boldsymbol{S} \odot \boldsymbol{\Xi}_m)(\mathbf{J}^{r_m} \otimes \mathbf{A}(\boldsymbol{\theta}_m))^{\dagger} + \sigma_v^2 \boldsymbol{I}_{N_R K} \tag{18}$$

$$\boldsymbol{\Theta}(\boldsymbol{W}) = \sigma_0^2 \mathbb{E}\Big[\Big((\mathbf{Diag}(\boldsymbol{p}(v_d)))^{\dagger} \otimes \boldsymbol{A}^{\dagger}(\boldsymbol{\theta}_0)\Big) \boldsymbol{W} (\mathbf{Diag}(\boldsymbol{p}(v_d)) \otimes \boldsymbol{A}(\boldsymbol{\theta}_0))\Big] \tag{19}$$

$$\overline{\boldsymbol{\Sigma}}_{dv}(\boldsymbol{W}) = \sum_{m=1}^{M} (\mathbf{J}^{r_m} \otimes \mathbf{A}(\boldsymbol{\theta}_m))^{\dagger} \big(\boldsymbol{W} \odot \overline{\boldsymbol{\Xi}}_m\big)(\mathbf{J}^{r_m} \otimes \mathbf{A}(\boldsymbol{\theta}_m)) + \frac{\sigma_v^2 \mathbf{tr}(\boldsymbol{W}) \mathbf{I}_{N_T K}}{\boldsymbol{E}}, \tag{20}$$

While $\boldsymbol{S} = \boldsymbol{s}\boldsymbol{s}^{\dagger} \in \mathbb{H}^{KN_T}$ and $\boldsymbol{W} = \boldsymbol{w}\boldsymbol{w}^{\dagger} \in \mathbb{H}^{KN_R}$, $\boldsymbol{\Xi}_m$ is given by (12), E denotes the energy of $\boldsymbol{s}$, $\overline{\boldsymbol{\Xi}}_m = \sigma_m^2 \boldsymbol{\Psi}_{\varepsilon_m}^{\overline{v}_{dm}} \otimes \boldsymbol{\Upsilon}_r$, $\boldsymbol{\Psi}_{\varepsilon_m}^{\overline{v}_{dm}}(k_1, k_2) = \Big(\boldsymbol{\Phi}_{\varepsilon_m}^{\overline{v}_{dm}}(k_1, k_2)\Big)^*$, $\forall (k_1, k_2) \in \{\mathbf{1}, \mathbf{2}, \cdots, K\}^2$ and $\boldsymbol{\Upsilon}_r = \mathbf{1}_r \mathbf{1}_r^T$ with $\mathbf{1}_r = [\mathbf{1}, \mathbf{1}, \cdots, \mathbf{1}]^T \in \mathbb{C}^{N_R}$, and $\mathbf{tr}(\cdot)$ denotes the trace of square matrix. These expressions follow from the results obtained in ([19], Appendix 3).

Note that $\boldsymbol{\Gamma}(\boldsymbol{S})$ and $\boldsymbol{\Theta}(\boldsymbol{W})$ can be rewritten in block matrix form, i.e.,

$$\boldsymbol{\Gamma}(\boldsymbol{S}) = \big(\sigma_0^2 \boldsymbol{\Gamma}_{m_1 m_2}\big)_{K \times K} \tag{21}$$

$$\boldsymbol{\Theta}(\boldsymbol{W}) = \big(\sigma_0^2 \boldsymbol{\Theta}_{i_1 i_2}\big)_{K \times K} \tag{22}$$

where $\boldsymbol{\Gamma}_{m_1 m_2} \in \mathbb{C}^{N_R \times N_R}$ and $\boldsymbol{\Theta}_{i_1 i_2} \in \mathbb{C}^{N_T \times N_T}$ can be computed by (38) and (46) respectively, $\forall (\boldsymbol{m}_1, \boldsymbol{m}_2, \boldsymbol{i}_1, \boldsymbol{i}_2) \in \{\mathbf{1}, \mathbf{2}, \cdots, \boldsymbol{K}\}^4$, as shown in Appendix **A**.

3.2. Constant modulus and similarity constraints

In practical applications, the designed STTC is enforced to be unimodular (i.e., constant modulus) since the nonlinear property of radar amplifiers [24, 25]. To this end, we limit the modulus of each element of the code $\boldsymbol{s}$ as a constant. Precisely, the $\boldsymbol{i}$th element $\boldsymbol{s}_i$ of $\boldsymbol{s}$ can be written as

$$\boldsymbol{s}_i = \frac{\mathbf{1}}{\sqrt{\boldsymbol{N}_T \boldsymbol{K}}} \boldsymbol{e}^{j\boldsymbol{\varphi}_i}, \boldsymbol{i} = \mathbf{1}, \mathbf{2}, \cdots, \boldsymbol{N}_T \boldsymbol{K}, \tag{23}$$

with $\boldsymbol{\varphi}_i$ denoting the phase of $\boldsymbol{s}_i$. Furthermore, $\boldsymbol{K}$ different similarity constraints are enforced on the $\boldsymbol{N}_T$ transmitting waveforms, namely

$$\|\boldsymbol{s}(\boldsymbol{k}) - \boldsymbol{s}_0(\boldsymbol{k})\|_{\infty} \le \boldsymbol{\xi}_k, \boldsymbol{k} = \mathbf{1}, \mathbf{2}, \cdots, \boldsymbol{K}, \tag{24}$$

where $\boldsymbol{s}_0(\boldsymbol{k}) \in \mathbb{C}^{N_T}$ is the reference code vector at the $\boldsymbol{k}$th transmission interval, $\boldsymbol{\xi}_k$ is a real parameter ruling the extent of the similarity, and $\|\boldsymbol{x}\|_{\infty}$ denotes the infinite norm.

Without loss of generality, we assume the same similarity parameter ξ_0 (i.e., $\xi_0 = \xi_1 = \cdots = \xi_K$) [12, 26, 28–30] on the sought STTC. Thus, Eq. (24) can be written as $\|s - s_0\|_\infty \le \xi_0$, where $s_0 = \left[s_0^T(1), \cdots, s_0^T(K)\right]^T$ is the reference code vector. Several reasons are presented to show the motivation to exploit the similarity constraints on radar codes. Actually, an arbitrary optimization of SINR via designing an STTC does not offer any kind of control on the shape of the resulting designed waveforms. Specifically, an pure optimization of the SINR can cause signals sharing high peak sidelobe levels and, in general, with an undesired ambiguity function feature. To this end, by exploiting the similarity constraint, when s_0 possesses suitable properties, such as low peak sidelobe levels, and reasonable Doppler resolutions, the designed STTC can enjoy some of the good ambiguity function feature of s_0. In other words, the similarity constraint compromises the performance between SINR improvement and suitable waveform features [31].

3.3. Design problem

Summarizing, the joint design of the STTC and the STRF can be formulated as the following constrained optimization problem:

$$\mathcal{P}_1 \begin{cases} \max\limits_{s,\,w} & \boldsymbol{\rho}(s, w) \\ \text{s.t.} & \|s(k) - s_0(k)\|_\infty \le \xi_k, k = 1, 2, \cdots, K, \\ & |s_i| = \dfrac{1}{\sqrt{N_T K}}, i = 1, 2, \cdots, N_T K, \\ & \|w\|^2 = 1, \end{cases} \tag{25}$$

where $|\cdot|$ and $\|\cdot\|$, respectively, represent the modulus and the Euclidean norm. Without loss of generality, we add the constraint $\|w\|^2 = 1$. $\mathcal{P}_1$ is a NP-hard problem [12, 28] whose optimal solution cannot be found in polynomial time. Next, we develop a new iterative algorithm to offer high-quality solution to the NP-hard problem (25).

4. STTC and STRF design procedure

This section focuses on the design of an iterative algorithm ensuring convergence properties, which is capable of offering high-quality solutions to the NP-hard problem $\mathcal{P}_1$ by sequentially improving the SINR. In particular, we exploit the pattern search framework to cyclically optimize the design variables $(w, s_1, s_2, \cdots, s_{N_T K})$.

4.1. STRF optimization

In this subsection, we deal with the STRF optimization for a fixed STTC s. Specifically, we handle the optimization problem

$$\mathcal{P}_w \begin{cases} \max\limits_{w} & \dfrac{w^\dagger \Gamma(ss^\dagger)w}{w^\dagger \Sigma_{dv}(ss^\dagger)w} \\ \mathbf{s.t.} & \|w\|^2 = \mathbf{1}. \end{cases} \tag{26}$$

We observe that the optimal solution w_o to $\mathcal{P}_w$ is the maximum eigenvector of the matrix

$$\left(\Sigma_{dv}(ss^\dagger)\right)^{-1}\Gamma(ss^\dagger),$$

i.e., to a generalized eigenvector of the matrices $\Gamma(s\,s^\dagger)$ and $\Sigma_{dv}(s\,s^\dagger)$ corresponding to the maximum generalized eigenvalue. Thus, a closed-form solution to $\mathcal{P}_w$ can be obtained by normalizing w_o.

4.2. STTC optimization

This subsection is devoted to the optimization of the STTC under a fixed STRF. Precisely, each code element in s is sequentially optimized under the fixed remaining N_TK-1 elements. Performing some algebraic manipulations to similarity constraints [26], the optimization problem $\mathcal{P}_{\bar{s}_i}$ with respect to the ith STTC variable, $i = 1, \ldots, N_TK$, is written by,

$$\mathcal{P}_{\bar{s}_i} \begin{cases} \max\limits_{\bar{s}_i} & \dfrac{s^\dagger \Theta(ww^\dagger)s}{s^\dagger \overline{\Sigma}_{dv}(ww^\dagger)s} \\ \mathbf{s.t.} & \arg\bar{s}_i \in [\gamma_i, \gamma_i+\delta], \\ & |\bar{s}_i| = \dfrac{1}{\sqrt{N_TK}}, \end{cases} \tag{27}$$

where $s = [s_1, s_2, \cdots, s_{i-1}, \bar{s}_i, s_{i+1}, \cdots, s_{KN_T}]^T$, $\gamma_i = \arg s_{0i} - \arccos\left(1-\xi^2/2\right)$, $\delta = 2\arccos(1-\xi^2/2)$, $\xi = \sqrt{N_TK}\xi_0$ with $0 \le \xi \le 2$, and s_{0i} is the ith element of s_0. Notice that for $\xi = 0$, the code s is equal to the reference code s_0, whereas the similarity constraint would become the constant modulus constraint with $\xi = 2$.

Remark: This procedure by resorting to pattern search framework offers a new strategy to address the code design problem under a fixed filter. In addition, this STTC optimization problem can be efficiently but approximatively settled by semidefinite relaxation (SDR) and randomization procedure with the computational complexity of $O\left((N_TK)^{3.5}\right) + O\left(L(N_TK)^2\right)$, where L is the number of randomization trials. However, the SDR technique usually shares a huge computational complexity, especially in large dimension N_TK, thus limiting its applications in real-time systems; moreover, the existing approach also needs the reasonable selection of L. On the other hand, it is shown that a higher quality solution can be further obtained via a sequential iteration optimization algorithm, which is capable of monotonically increasing the SINR value and achieving a stationary point of the formulated NP-hard problem [27].

Next, we focus on the proposed iteration algorithm to solve problem (27) in a polynomial time. In particular, performing some algebraic manipulations to the objective function in (27), $\mathcal{P}_{\bar{s}_i}$

can be equivalently rewritten as a fractional programming optimization problem by the following proposition.

Proposition 4.1 *The problem* $\mathcal{P}_{\bar{\mathbf{s}}_i}$ *is equivalent to*

$$\begin{cases} \max\limits_{\bar{s}_i} & \dfrac{\Re(a_{1,i}\bar{s}_i)+a_{3,i}}{\Re(b_{1,i}\bar{s}_i)+b_{3,i}} \\ \mathbf{s.t.} & \bar{s}_i = \dfrac{1}{\sqrt{N_T K}} e^{j\varphi}, \varphi \in [\gamma_i, \gamma_i+\delta], \end{cases} \tag{28}$$

where

$$a_{3,i} = \frac{a_{0,i}}{N_T K}+a_{2,i}, b_{3,i} = \frac{b_{0,i}}{N_T K}+b_{2,i}, \tag{29}$$

and $a_{k,i}, b_{k,i}$ *are constants for* $k = 0, 1, 2$, $\Re(x)$ *denotes the real part of* x.

Proof. See Appendix **B**.

Problem (28) is solvable [32] since the objective function is continuous with $\Re(b_{1,i}\bar{s}_i)+b_{3,i}>0$ and the constraint is a compact set (closed and bounded set of $\mathbb{C}$). Thus, we consider the following parametric problem [32],

$$\begin{cases} \max\limits_{\bar{s}_i} & \varrho(\mu) = \{\Re(a_{1,i}\bar{s}_i)+a_{3,i}-\mu[\Re(b_{1,i}\bar{s}_i)+b_{3,i}]\} \\ \mathbf{s.t.} & \bar{s}_i = \dfrac{1}{\sqrt{N_T K}} e^{j\varphi}, \varphi \in [\gamma_i, \gamma_i+\delta]. \end{cases} \tag{30}$$

After some simple manipulations, problem (30) can be rewritten as

$$\begin{cases} \max\limits_{\bar{s}_i} & \Re(c_i\bar{s}_i) \\ \mathbf{s.t.} & \bar{s}_i = \dfrac{1}{\sqrt{N_T K}} e^{j\varphi}, \varphi \in [\gamma_i, \gamma_i+\delta], \end{cases} \tag{31}$$

where $c_i = a_{1,i}-\mu b_{1,i}$ and the constant $a_{3,i}-\mu b_{3,i}$ do not affect the optimal value.

Interestingly, problem (31) shares a closed-form solution whose phase φ^* is given by,

$$\varphi^* = -\varphi_{c_i}, -\varphi_{c_i} \in [\gamma_i, \gamma_i+\delta],$$

where φ_{c_i} is the phase of c_i; otherwise, the optimal solution φ^* is given by,

$$\varphi^* = \begin{cases} \gamma_i+\delta & \cos\left(\varphi_{c_i}+\gamma_i+\delta\right) \geq \cos\left(\varphi_{c_i}+\gamma_i\right) \\ \gamma_i & \cos\left(\varphi_{c_i}+\gamma_i+\delta\right) < \cos\left(\varphi_{c_i}+\gamma_i\right). \end{cases} \tag{32}$$

We observe that problems (28) and (30) are relevant in each other via Lemma 2.1 of [32]. Specifically, we can find a solution to problem (28) by obtaining a solution of the equation

$\varrho(\mu) = \mathbf{0}$ concerning $\bar{s}_i$. To this end, the Dinkelbach-type procedure [32, 33] summarized in Algorithm 1 is introduced to solve problem (27).

Algorithm 1. Dinkelbach-type algorithm for solving $\mathcal{P}_{\bar{s}_i}$

Input: $a_{1,i}$, $a_{3,i}$, $b_{1,i}$, $b_{3,i}$, γ_i and δ;

Output: An optimal solution $\hat{s}_i$ to $\mathcal{P}_{\bar{s}_i}$;

1. Randomly generate $\bar{s}_{i,0}$ within the feasible sets;
2. Compute $\mu_1 = \frac{\Re\left(a_{1,i}\bar{s}_{i,0}\right)+a_{3,i}}{\Re\left(b_{1,i}\bar{s}_{i,0}\right)+b_{3,i}}$ and let $k := 1$;
3. Find the optimal solution $\bar{s}_{i,k}$ by solving problem (30),
4. If $\varrho(\mu_k) = \mathbf{0}$, then $\bar{s}_{i,k}$ is an optimal solution of $\mathcal{P}_{\bar{s}_i}$ with optimal value μ_k and stop. Otherwise, go to step 5;
5. Let $\mu_k = \frac{\Re\left(a_{1,i}\bar{s}_{i,k}\right)+a_{3,i}}{\Re\left(b_{1,i}\bar{s}_{i,k}\right)+b_{3,i}}$ and $k := k+1$; Then go to step 2.

Algorithm 1 sharing a linear convergence rate [34] is needed to handle the problem (30) in each iteration. The objective value of the generated sequence of points has a monotonic convergence property, and the optimal value of (28) can be achieved eventually. We set the exit condition $\varrho(\mu) = \mathbf{0}$, actually, which can be replaced by $\varrho(\mu) \le \varsigma$, with ς being a prescribed accuracy.

4.3. Transmit-receive system design

This subsection reports the iteration optimization procedure for the STTC and STRF in Algorithm 2. In particular, Algorithm 2 guarantees that the SINR monotonically increases[2]. Furthermore, we need to point out that the maximum block improvement (MBI) [24] framework could be used to ensure the convergence to a stationary point of problem $\mathcal{P}_1$.

The global computation consume of the Algorithm 2 is linear to the number of iterations and polynomial with the sizes of the STTC and the STRF. More specifically, each iteration of the proposed algorithm involves the computational cost associated with the solution to problems (26) and $\mathcal{P}_{\bar{s}_i}$, for $i = 1, 2, \cdots, N_T K$. The former requires to solve the generalized eigenvalue decomposition with the order of $O\left((N_R K)^3\right)$ (see [35], p. 500). Similarly, the latter is linear to polynomial with the size of the STTC, while each iteration needs the solution of a generalized fractional programming problem with the computational complexity of $O\left((N_T K)^2\right)$. We need to point out that SOA2, based on the SDR and randomization method, can also be used to the solution of problem (25). However, it cannot guarantee the convergence to a stationary point due to the use of randomized approximations. Moreover, from computational complexity, each iteration of SOA2 has the order of $O\left((N_R K)^3\right) + O\left((N_T K)^{3.5}\right) + O\left(L(N_T K)^2\right)$, whereas Algorithm 2 is $O\left((N_R K)^3\right) + O\left((N_T K)^3\right)$.

[2]Notice that the similar convergence analysis can be obtained in [23].

Algorithm 2. Algorithm for the joint STTC $\boldsymbol{s}$ and STRF $\boldsymbol{w}$ design

Input: $\overline{\theta}_0$, ϑ_0, s_0, ξ, σ_m, r_m, $\overline{v}_{d_m}$, ε_m, for $m = 0, 1, \cdots, M$, and θ_p, for $p = 1, 2, \cdots, M$;

Output: An optimal solution (s^*, w^*) to $\mathcal{P}_1$;

1. Construct γ_m, δ, $m = 1, 2, \cdots, N_T K$ exploiting s_0;
2. For $n = 0$ and initialize $s^{(n)} = s_0$;
3. Compute $w^{(0)} = \frac{w_o^{(0)}}{\|w_o^{(0)}\|}$ and $\rho_0 = \rho\left(s^{(0)}, w^{(0)}\right)$;
4. $n := n+1$ and $i = 0$;
5. Compute $\overline{\Sigma}_{dv}\left(w^{(n)} w^{(n)\dagger}\right)$ and $\Theta\left(w^{(n)} w^{(n)\dagger}\right)$ by (20) and (22), respectively;
6. $i := i+1$;
7. Compute $a_{k,i}$ and $b_{k,i}$ by (50) and (51), $k = 0, 1, 2$, respectively;
8. Find $a_{3,i}$ and $b_{3,i}$ by (29);
9. Exploit **Algorithm 1** to update s_i by maximizing the problem (27);
10. If $i = N_T K$, output $s^{(n)} = [s_1, s_2, \cdots, s_{KN_T}]^T$. Otherwise, return to step 7;
11. Compute $\Sigma_{dv}\left(s^{(n)} s^{(n)\dagger}\right)$ and $\Gamma\left(s^{(n)} s^{(n)\dagger}\right)$ by (18) and (21), respectively;
12. Find the generalized eigenvector $w_o^{(n)}$ of matrices $\Gamma\left(s^{(n)} s^{(n)\dagger}\right)$ and $\Sigma_{dv}\left(s^{(n)} s^{(n)\dagger}\right)$ corresponding to the maximum generalized eigenvalue;
13. Compute $w^{(n)} = \frac{w_o^{(n)}}{\|w_o^{(n)}\|}$ and $\rho_n = \rho\left(s^{(n)}, w^{(n)}\right)$;
14. If $|\rho_n - \rho_{n-1}| \le \kappa$, where κ is a user selected parameter to control convergence, output $s^* = s^{(n)}$ and $w^* = w^{(n)}$; Otherwise, repeat step 5 until convergence.

5. Numerical results

This section focuses on assessing the capability of the proposed algorithm for designing optimized STTC and STRF in signal-dependent interference for both a nonuniform and an uniform point-like clutter environment. In particular, for both scenarios, we consider an L-band radar with operating frequency $f_c = 1.4$ GHz, which is equipped with an ULA of $N_T = 4$ transmit elements and $N_R = 8$ receive elements under an interelement spacing $d_t = d_r = \lambda/2$. We set the code length $K = 13$ for each transmitter and the orthogonal linear frequency modulation (LFM[3]) is used as the reference waveform s_0 [12] with the (n_t, k)th entry of the reference $S^{(0)}$ given by,

[3]Notice that LFM waveforms have good properties in the pulse compression and ambiguity feature.

$$S^{(0)}(n_t,k)=\frac{\exp\left\{j2\pi n_t(k-1)/N_T\right\}\exp\left\{j\pi(k-1)^2/N_T\right\}}{\sqrt{KN_T}} \tag{33}$$

where $n_t=1,2,\cdots,N_T$ and $k=1,2,\cdots,K$. Hence, the reference code is derived as $s_0=vec\left(S^{(0)}\right)$. Moreover, we assume the target located at range-azimuth bin of interest (0,0) with power $\sigma_0^2=10$ dB. In addition, we set a mean azimuth $\overline{\theta}_0=0^\circ$ with azimuth uncertainty $\vartheta/2=1^\circ$, and a normalized mean Doppler frequency $\overline{v}_{d_0}=0.4$ with Doppler uncertainty $\varepsilon_0/2=0.04$ for the presence of target. We set the noise variance to $\sigma_v^2=0$ dB. Finally, the exit condition[4] $\varsigma=10^{-3}$ for Algorithms 1 and 2 is $\kappa=10^{-3}$, i.e.,

$$|\rho_n-\rho_{n-1}|\le 10^{-3}. \tag{34}$$

All simulations are performed using Matlab 2010a version, running on a standard PC (with a 3.3 GHz Core i5 CPU and 8 GB RAM).

5.1. Nonuniform point-like clutter environment

This subsection focuses on a scenario where three disturbances, respectively, are located at the spatial angles $\theta_1=-55^\circ,\theta_2=-20^\circ,\theta_3=40^\circ$, with corresponding range bins $r_i=0,i=1,2,3$ and powers $\sigma_1^2=30\text{dB}$, $\sigma_2^2=28\text{dB}$, $\sigma_3^2=25$ dB. Moreover, we suppose $\overline{v}_{d_1}=-0.35$, $\overline{v}_{d_2}=-0.15$, $\overline{v}_{d_3}=0.25,\varepsilon_m/2=0.04,m=1,2,3$ for the presence of the disturbances.

For comparison purpose, we also perform simulations for the SOA2 with constant modulus and similarity constraints as well as the algorithm in [19] with energy constraint (i.e., $\|s\|^2=1$), respectively. In particular, **Figure 2** shows the SINR versus the iteration number for different ξ by also comparing the results obtained via Algorithm 2 and SOA2 considering L = 100 and exploiting the CVX toolbox [36] to handle the semidefinite programming (SDP) involved in SOA2. The results exhibit that the SINR values achieved using Algorithm 2 and SOA2 increase as the iteration number increases. In addition, the SINR increases as ξ increases owing to the higher degrees of freedom available at the design stage. Precisely, Algorithm 2 is superior to SOA2 for $\xi=0.1,0.5,1.3$. It is interesting to note that Algorithm 2 and SOA2 share almost the same SINR for $\xi=2$, whereas both obtain lower SINR than the case considering energy constraint. Finally, it is worth pointing out that a loss of SINR caused by constant constraint can be observed since the gap of SINR between $\xi=2$ and energy constraint is about 1 dB.

Table 1 reports the achieved SINR values, iterations number, and global computation time of Algorithm 2 and SOA2 supposing a target with $-\pi/180\le\theta_0\le\pi/180$, $0.36\le v_{d_0}\le 0.44$ for $\xi=0.1,0.5,1.3,2$ and setting the same exit condition for SOA2. We observe that Algorithm 2 and SOA2 both converge very fast. Additionally, Algorithm 2 is superior to SOA2 concerning

[4]Notice that we consider the exit condition $A/10^4$ both for Algorithms 1 and 2, where A denotes the upper bound of the objective function neglecting the signal-dependent interference (for example, $A=10$ is considered in this simulation).

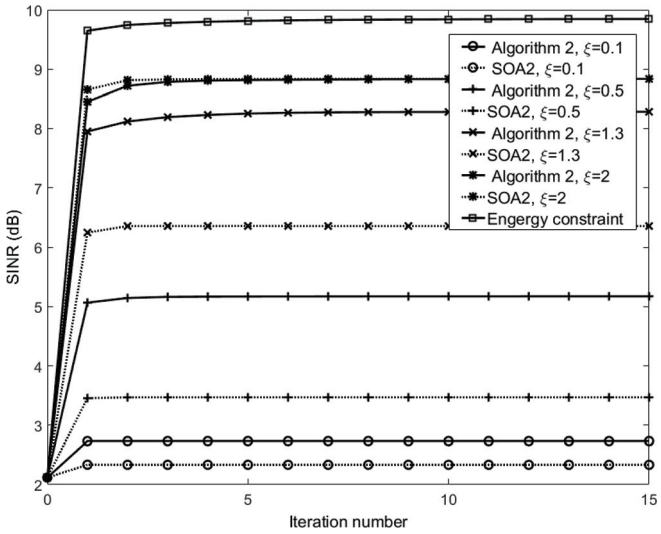

Figure 2. The SINR behavior versus iteration number assuming a target with $-\pi/180 \le \theta_0 \le \pi/180$, $0.36 \le v_{d_0} \le 0.44$ for $\xi = 0.1, 0.5, 1.3, 2$, s_0 as the initial point.

Algorithm 2				**SOA2**		
ξ	SINR	n	Time	SINR	n	Time
0.1	2.7	2	0.3236	2.3	3	4.0145
0.5	5.2	6	0.8942	3.5	3	3.9688
1.3	8.3	12	1.7175	6.3	4	5.3498
2	8.8	13	1.8102	8.8	7	9.3621

Table 1. SINR values (in dB), iterations number, and global computation time (in seconds) of Algorithm 2 and SOA2 assuming a target with $-\pi/180 \le \theta_0 \le \pi/180$, $0.36 \le v_{d_0} \le 0.44$ for $\xi = 0.1, 0.5, 1.3, 2$, s_0 as the initial point.

the achieved SINR value for $\boldsymbol{\xi = 0.1, 0.5, 1.3}$ and concerning the required computational cost for $\boldsymbol{\xi = 0.1, 0.5, 1.3, 2}$.

In the following, the joint frequency and azimuth behavior of STTC and STRF are considered corresponding to $\boldsymbol{\xi = 2}$ supposing $\boldsymbol{-\pi/180 \le \theta_0 \le \pi/180}$, $\boldsymbol{0.36 \le v_{d_0} \le 0.44}$ for different iteration numbers, by using the contour map of the slow-time cross ambiguity function (CAF) [19],

$$g^{(n)}\left(s^{(n)}, w^{(n)}, r, v, \theta\right) = \left| w^{(n)\dagger} \mathbf{P}_r \widehat{\mathbf{A}}(v, \theta) s^{(n)} \right|^2, \tag{35}$$

where $\widehat{\mathbf{A}}(v, \theta)$ and $\mathbf{P}_r$ are obtained by exploiting Eqs. (6) and (8), respectively. **Figure 3** plots the contour map of the Doppler-azimuth plane of CAF at $\boldsymbol{r = 0}$ versus the iteration number $\boldsymbol{n = [0, 1, 4, 15]}$ for Algorithm 2. As expected, the lower and lower values in the regions of (highlighted by black ellipses) $\boldsymbol{\theta_1 = -55^\circ}$ and $\boldsymbol{-0.39 \le v \le -0.31}$, $\boldsymbol{\theta_2 = -20^\circ}$ and $\boldsymbol{-0.19 \le v \le}$

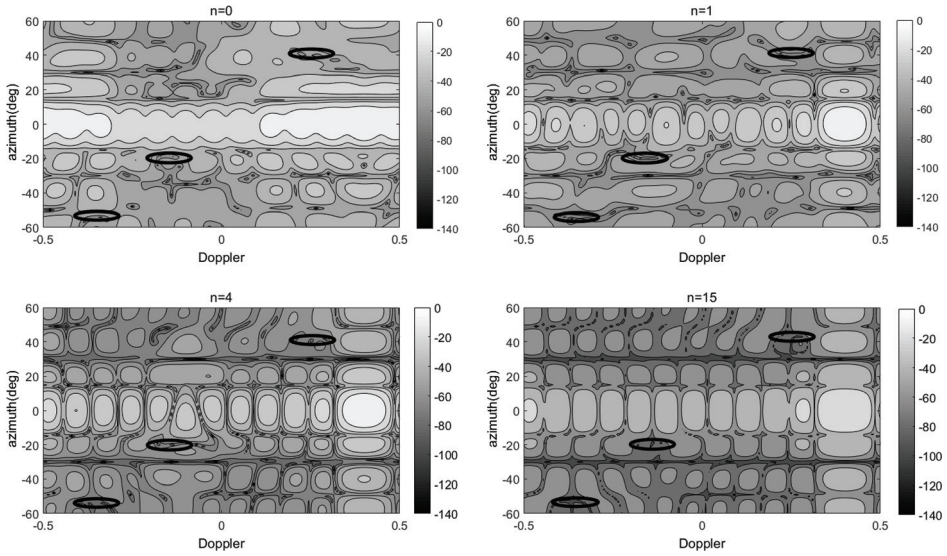

Figure 3. Doppler-azimuth plane of CAF at $r = 0$ for $\xi = 2$ of Algorithm 2 for $n = [0, 1, 4, 15]$ assuming a target with $-\pi/180 \le \theta_0 \le \pi/180$, $0.36 \le v_{d_0} \le 0.44$ (black ellipses represent the locations of three interference sources), s_0 as the initial point.

$-\mathbf{0.11}$, and $\boldsymbol{\theta_3 = 40^\circ}$ and $\mathbf{0.21 \le v \le 0.29}$ are achieved, with the increase of $\boldsymbol{n}$. Thus, it is worth pointing out that the proposed algorithm can suitably shape the CAF to resist interferences.

For the uniform distribution, we define both standard deviations $\sigma_{v_{d_0}}$ and σ_{θ_0} of target Doppler and azimuth as, respectively,

$$\sigma_{v_{d_0}} = \varepsilon_0/\sqrt{12}, \sigma_{\theta_0} = \vartheta_0/\sqrt{12}.$$

Figure 4 shows the SINR behaviors versus the standard deviations $\sigma_{v_{d_0}}$ (**Figure** 4**a**) and σ_{θ_0} (**Figure** 4**b**) supposing $\overline{\theta}_0 = 0^\circ$, $\overline{v}_{d_0} = 0.4$, respectively. Our curves highlight that the proposed algorithm can further improve SINR gain in comparison with SOA2 for $\xi = 0.1, 0.5, 1.3$. We also observe that the higher $\sigma_{v_{d_0}}$ and σ_{θ_0} and the lower SINR can be obtained due to the larger inaccuracies on the knowledge of Doppler and azimuth of the actual target. Finally, we need to point out that the proposed design procedure still has the better robustness against a large uncertain set in comparison with SOA2.

5.2. Uniform clutter environment

This subsection focuses on a scenario where we consider a homogeneous range-azimuth ground clutter interfering with the range-azimuth bin of interest (0,0). Specifically, for each range-azimuth ground clutter bin, a clutter to noise ratio (CNR) of 25 dB and a normalized Doppler frequency $\overline{v} = 0$ with Doppler uncertainty $\varepsilon/2 = 0.04$ are considered. We suppose

$M = 50$ range-azimuth ground clutter bins located within the azimuth angular sector $[-\pi/2, \pi/2]$. Moreover, we set the range ring $r_i = 0$ for all range-azimuth ground clutter bins.

In **Figure 5**, we show the SINR of Algorithm 2 and SOA2 for $\xi = 0.1, 0.5, 1.3, 2$ supposing a target $-\pi/180 \le \theta_0 \le \pi/180$, $0.36 \le v_{d_0} \le 0.44$. The SINR values increases both for Algorithm 2 and SOA2 with the increasing iteration number n. Furthermore, we observe the higher ξ, the better SINR values reflecting the larger and larger feasible set. Interestingly, Algorithm 2 significantly outperforms SOA2 for all the considered ξ, except for $\xi = 2$ where they both

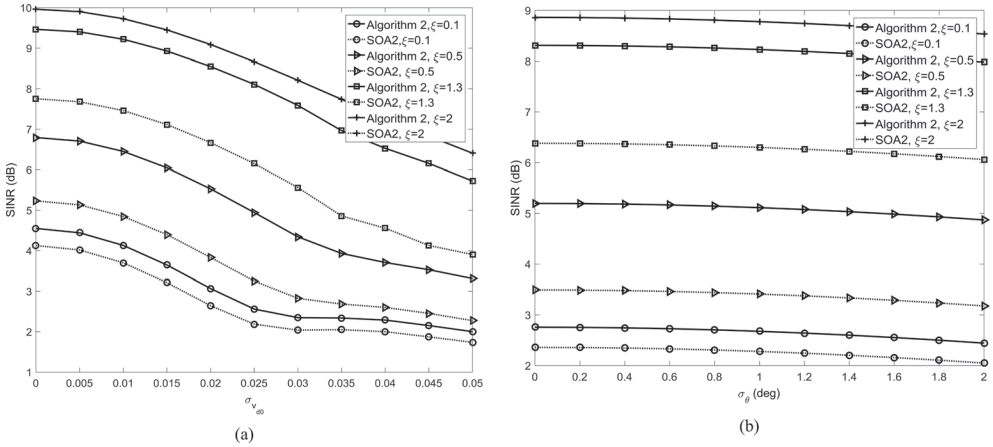

Figure 4. The SINR behaviors versus the standard deviations $\sigma_{v_{d_0}}$ (**Figure 4a**) and σ_{θ_0} (**Figure 4b**) of Doppler and azimuth of target with $\overline{\theta}_0 = 0^\circ$, $\overline{v}_{d_0} = 0.4$ considering $\xi = 0.1, 0.5, 1.3, 2$, respectively, s_0 as the initial point.

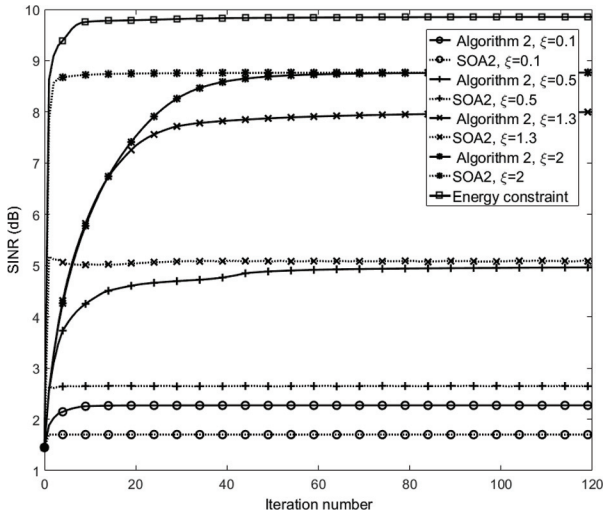

Figure 5. The SINR behavior versus iteration number assuming a target with $-\pi/180 \le \theta_0 \le \pi/180$, $0.36 \le v_{d_0} \le 0.44$ in uniform clutter environment for $\xi = 0.1, 0.5, 1.3, 2$, s_0 as the initial point.

achieve the same SINR value. In particular, we see that the gap between $\xi = \mathbf{2}$ and energy constraint is about 1.1 dB because of the introduction of constant modulus constraint. We also observe that in this scenario, Algorithm 2 needs a higher number of iterations to achieve convergence compared with that in **Figure 2**. For instance, for $\xi = \mathbf{0.1}$, Algorithm 2 converges with about 12 iterations in **Figure 5**, whereas in **Figure 2** after about 2 iterations.

In **Table** 2, we summarize the SINR values, iterations number, and the global computation time of Algorithm 2 and SOA2. In particular, Algorithm 2 shows a lower computational time for $\xi = \mathbf{0.1, 2}$. Furthermore, it is observed that the gains of 2.3 and 3 dB are achieved using Algorithm 2 with a slightly higher computational cost for $\xi = \mathbf{0.5, 1.3}$, respectively.

Figure 6 shows the joint frequency and azimuth behavior of STTC and STRF concerning CAF. Specifically, the contour map of the Doppler-azimuth plane of CAF at $\boldsymbol{r} = \mathbf{0}$ against the

Algorithm 2				**SOA2**		
ξ	SINR	n	Time	SINR	n	Time
0.1	2.3	12	2.6325	1.7	3	4.3007
0.5	4.9	68	13.0183	2.6	8	11.4606
1.3	8.0	120	21.4875	5.0	10	14.5547
2	8.8	82	15.8699	8.8	24	35.0873

Table 2. SINR values (in dB), iterations number, and global computation time (in seconds) of Algorithm 2 and SOA2 assuming a target with $-\pi/180 \leq \theta_0 \leq \pi/180$, $0.36 \leq v_{d_0} \leq 0.44$ in uniform clutter environment for $\xi = 0.1, 0.5, 1.3, 2$, s_0 as the initial point.

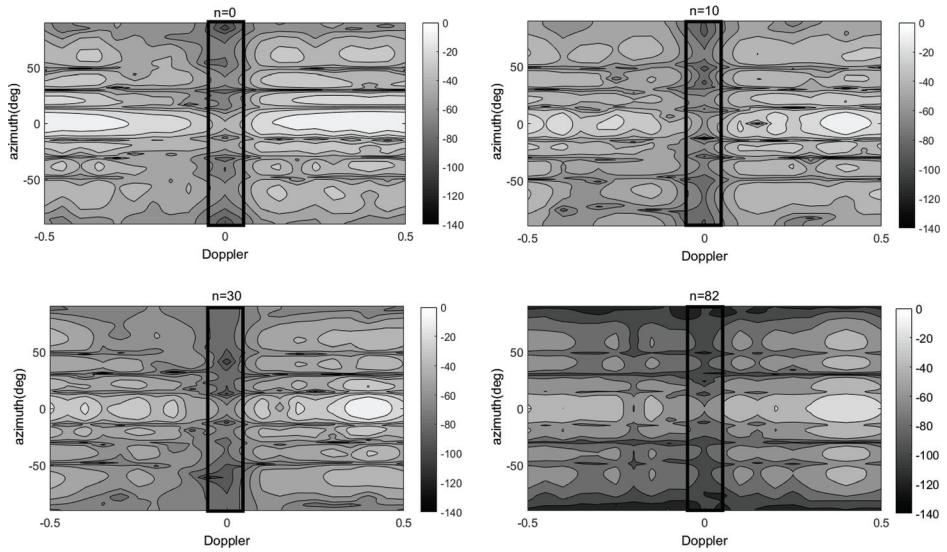

Figure 6. Doppler-azimuth plane of CAF at $r = 0$ for $\xi = 2$ of Algorithm 2 for $n = [0, 10, 30, 82]$ assuming a target with $-\pi/180 \leq \theta_0 \leq \pi/180$, $0.36 \leq v_{d_0} \leq 0.44$ in uniform clutter environment (black rectangles represent the locations of uniform clutter), s_0 as the initial point of Algorithm 2 and SOA2.

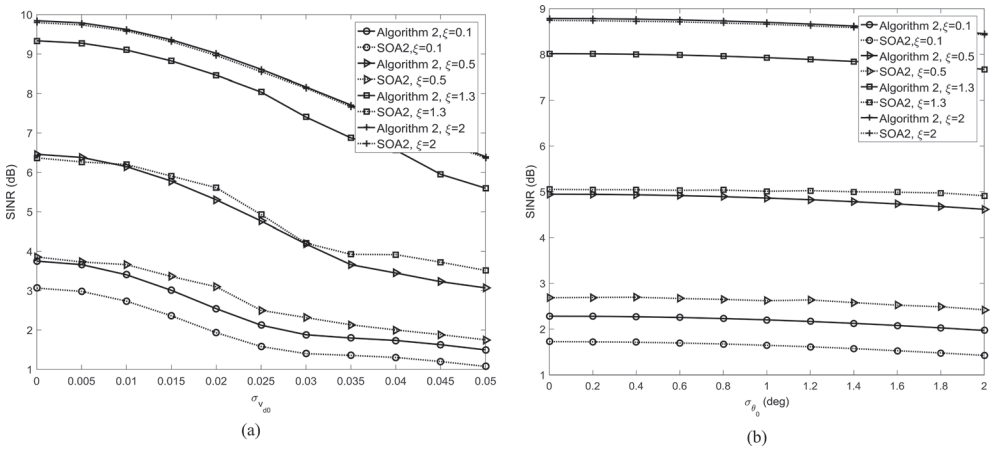

Figure 7. The SINR behaviors versus the standard deviations $\sigma_{v_{d_0}}$ (a) and σ_{θ_0} () of Doppler and azimuth of target with $\overline{\theta}_0 = 0^\circ$, $\overline{v}_{d_0} = 0.4$, respectively, s_0 as the initial point of Algorithm 2 and SOA2.

iteration number ($\boldsymbol{n} = [\mathbf{0}, \mathbf{10}, \mathbf{30}, \mathbf{82}]$) considering $\boldsymbol{\xi} = \mathbf{2}$ for Algorithm 2 is plotted. We observe that $\boldsymbol{g}^{(n)}\left(\boldsymbol{s}^{(n)}, \boldsymbol{w}^{(n)}, \boldsymbol{r}, \boldsymbol{v}, \boldsymbol{\theta}\right)$ obtains lower and lower values in the region of $-\boldsymbol{\pi/2} \leq \boldsymbol{\theta} \leq \boldsymbol{\pi/2}$, $-\mathbf{0.04} \leq \boldsymbol{v} \leq \mathbf{0.04}$ (highlighted by black rectangles) with the increase of iteration number $\boldsymbol{n}$. This performance behavior highlights that the proposed algorithm of joint design STTC and STRF possesses the ability of sequentially refining the shape of the CAF to achieve better and better clutter suppression levels.

Figure 7 plots the SINR versus the standard deviations $\sigma_{v_{d_0}}$ (**Figure** 7**a**) and σ_{θ_0} (**Figure** 7**b**) of Doppler and azimuth of target with $\overline{\boldsymbol{\theta}}_{\mathbf{0}} = \mathbf{0}^\circ$, $\overline{\boldsymbol{v}}_{\boldsymbol{d}_0} = \mathbf{0.4}$, respectively. Again, we see that Algorithm 2 obtains a higher SINR gain than SOA2 for $\boldsymbol{\xi} = \mathbf{0.1, 0.5, 1.3}$, whereas they both fulfill the near same gain at $\boldsymbol{\xi} = \mathbf{2}$. Interestingly, we also observe that a decreasing trend in gain with the increase in standard deviation. This is reasonable due to that the larger standard deviation results in the larger uncertainty on the knowledge of target.

6. Conclusions

This chapter has considered the joint STTC and STRF design for MIMO radar under signal-dependent interference. We focus on a narrow band colocated MIMO radar with a moving point-like target considering imprecise a prior knowledge including Doppler and azimuth. Summarizing,

- We have devised an iterative algorithm to maximize the SINR accounting for both a similarity constraint and constant modulus requirements on the probing waveform. Each iteration of the algorithm requires the solution of hidden convex problems. The consequent computational complexity is linear with the number of iterations and polynomial with the sizes of the STTC and the STRF.

- We have assessed the performance of the proposed iteration algorithm through numerical simulations. The results have manifested that the larger the similarity parameter (i.e., the weaker the similarity constraint), the larger the output SINR due to the expanded feasible set. Moreover, we observed that the devised iteration procedure can provide a monotonic improvement of SINR and ensuring convergence to a stationary point, which possesses excellent superiority in computation complexity and performance gain compared with the related SOA2. The numerical examples also have revealed the capability of the developed procedure to sequentially refine the shape of the CAF both in nonuniform point-like clutter environment and uniform clutter environment.

Possible future work tracks might extend the proposed framework to consider spectral constraint [37] and MIMO radar beampattern design by optimizing integrated sidelobe level (ISL) with practical constraints.

Acknowledgements

This work was supported by the National Natural Science Foundation of China under Grants 61771109 and 61501083. The authors like to thank Dr. Augusto Aubry for his constructive comments.

Appendices

Appendix A: Computation of $\boldsymbol{\Gamma(S)}$ and $\boldsymbol{\Theta(W)}$

Let us denote $\boldsymbol{S}$ in block matrix form, i.e.,

$$\boldsymbol{S} = (\boldsymbol{S}_{n_1 n_2})_{K\times K}, \tag{36}$$

where the block matrix $\boldsymbol{S}_{n_1 n_2} \in \mathbb{C}^{N_T \times N_T}$ can be computed as

$$\boldsymbol{S}_{n_1 n_2} = \boldsymbol{s}(\boldsymbol{n_1})\boldsymbol{s}^{\dagger}(\boldsymbol{n_2}),\ (\boldsymbol{n_1}, \boldsymbol{n_2}) \in \{\mathbf{1}, \mathbf{2}, \cdots, \boldsymbol{K}\}^{\mathbf{2}}. \tag{37}$$

Hence, exploiting the fact that $\boldsymbol{v}_{d_0}$ and $\boldsymbol{\theta_0}$ are statistically independent random variables, the block matrix $\boldsymbol{\Gamma}_{m_1 m_2}$ of $\boldsymbol{\Gamma(S)}$ in (21) can be expressed as

$$\boldsymbol{\Gamma}_{m_1 m_2} = \sigma_0^2 \mathbb{E}\left[e^{j2\pi(m_1-m_2)v_{d_0}}\right] \mathbb{E}\left[\boldsymbol{A}(\boldsymbol{\theta_0})\boldsymbol{S}_{m_1 m_2}\boldsymbol{A}^{\dagger}(\boldsymbol{\theta_0})\right],\ (\boldsymbol{m_1}, \boldsymbol{m_2}) \in \{\mathbf{1}, \mathbf{2}, \cdots, \boldsymbol{K}\}^{\mathbf{2}}. \tag{38}$$

Since $\boldsymbol{v}_{d_0}$ is a uniformly distributed random variable, e.g., $\boldsymbol{v}_{d_0} \sim \boldsymbol{U}\left(\overline{\boldsymbol{v}}_{d_0} - \frac{\boldsymbol{\varepsilon_0}}{\mathbf{2}}, \overline{\boldsymbol{v}}_{d_0} + \frac{\boldsymbol{\varepsilon_0}}{\mathbf{2}}\right)$, the first expectation of (38) can be computed as

$$\mathbb{E}\left[e^{j2\pi(m_1-m_2)v_{d_0}}\right] = \frac{\mathbf{1}}{\boldsymbol{\varepsilon_0}} \int_{\overline{v}_{d_0}-\frac{\varepsilon_0}{2}}^{\overline{v}_{d_0}+\frac{\varepsilon_0}{2}} e^{j2\pi(m_1-m_2)v_{d_0}} dv_{d_0} = e^{j2\pi\overline{v}_{d_0}(m_1-m_2)} \frac{\mathbf{sin}\left[\pi\varepsilon_0(m_1-m_2)\right]}{\pi\varepsilon_0(m_1-m_2)}, (\boldsymbol{m_1}, \boldsymbol{m_2}) \in \{\mathbf{1}, \mathbf{2}, \cdots, \boldsymbol{K}\}^{\mathbf{2}}. \tag{39}$$

Let $\boldsymbol{\Phi}_{\vartheta_0}^{\overline{\theta}_0}$ denote the second expectation of (38) whose $(\boldsymbol{q_1}, \boldsymbol{q_2})$ entry is given by

$$\boldsymbol{\Phi}_{\vartheta_0}^{\overline{\theta}_0}(q_1,q_2) \quad = \mathbb{E}\left[\tilde{a}_{q_1}^T(\theta_0) S_{m_1m_2} \tilde{a}_{q_2}^*(\theta_0)\right] = tr\left(S_{m_1m_2}\overline{\boldsymbol{\Phi}}_{q_1q_2}\right), \qquad (q_1,q_2) \in \{1,2,\cdots,N_R\}^2, \quad (40)$$

where

$$\tilde{a}_q(\theta_0) = \frac{1}{\sqrt{N_R}} e^{-j\frac{2\pi \sin\theta_0}{\lambda} d_r(q-1)} a_t{}^*(\theta_0), \quad q \in \{1,2,\cdots,N_R\}, \quad (41)$$

and

$$\overline{\boldsymbol{\Phi}}_{q_1q_2} = \mathbb{E}\left[\tilde{a}_{q_2}^*(\theta_0)\tilde{a}_{q_1}^T(\theta_0)\right]. \quad (42)$$

Based on θ_0 as a uniformly distributed random variable, e.g., $\theta_0 \sim \boldsymbol{U}(\overline{\theta}_0 - \frac{\vartheta_0}{2}, \overline{\theta}_0 + \frac{\vartheta_0}{2})$, the (q_1,q_2) entry of expectation $\overline{\boldsymbol{\Phi}}_{q_1q_2}$ can be computed as

$$\overline{\boldsymbol{\Phi}}_{q_1q_2}(p_1,p_2) = \frac{1}{N_T N_R \vartheta_0} \int_{\overline{\theta}_0 - \frac{\vartheta_0}{2}}^{\overline{\theta}_0 + \frac{\vartheta_0}{2}} e^{j\frac{2\pi \sin\theta_0}{\lambda}\left[d_r(q_2-q_1)+d_t(p_1-p_2)\right]} d\theta_0 (q_1,q_2) \in \{1,2,\cdots,N_R\}^2, \ (p_1,p_2) \in \{1,2,\cdots,N_T\}^2. \quad (43)$$

As to the computation of (43), we can adopt numerical integration.

Next, we focus on the computation of $\boldsymbol{\Theta}(W)$. Similarly, let us write W in block matrix structure, given by

$$W = (W_{i_1i_2})_{K\times K}, \quad (44)$$

where block matrix $W_{i_1i_2} \in \mathbb{C}^{N_R \times N_R}$ is given by

$$W_{i_1i_2} = w(i_1) w^\dagger(i_2), \qquad (i_1,i_2) \in \{1,2,\cdots,K\}^2. \quad (45)$$

As a consequence, based on the statistical independence of v_{d_0} and θ_0, the block matrix $\boldsymbol{\Theta}_{i_1i_2}$ of $\boldsymbol{\Theta}(W)$ in (22) is

$$\boldsymbol{\Theta}_{i_1i_2} = \sigma_0^2 \mathbb{E}\left[e^{-j2\pi(i_1-i_2)v_{d_0}}\right] \mathbb{E}\left[A^\dagger(\theta_0) W_{i_1i_2} A(\theta_0)\right], \qquad (i_1,i_2) \in \{1,2,\cdots,K\}^2. \quad (46)$$

Following the same lines of reasoning in (39) and (43), both expectations in (46) can be evaluated.

Appendix B: Proof of (25)

The $\boldsymbol{\Theta}(w\,w^\dagger)$ can be rewritten as

$$\boldsymbol{\Theta}(ww^\dagger) = [a_1, a_2, \cdots, a_{KN_T}], \quad (47)$$

where $a_n = [\alpha_{n,1}, \alpha_{n,2}, \cdots, \alpha_{n,KN_T}]^T \in \mathbb{C}^{KN_T}$, for $n = 1, 2, \cdots, KN_T$. Hence, the $s^\dagger \boldsymbol{\Theta}(ww^\dagger)s$ can be expressed as

$$\bar{s}^{\dagger}\Theta(ww^{\dagger})\bar{s}=\sum_{\substack{n=1\\n\neq i}}^{KN_T}\bar{s}^{\dagger}a_n s_n+\bar{s}^{\dagger}a_i\bar{s}_i=\sum_{\substack{n=1\\n\neq i}}^{KN_T}\bar{s}_i^{*}\alpha_{n,i}s_n+\bar{s}^{\dagger}a_i\bar{s}_i+\sum_{\substack{k=1\\k\neq i}}^{KN_T}\sum_{\substack{l=1\\l\neq i}}^{KN_T}s_l^{*}\alpha_{k,l}s_k. \tag{48}$$

Using the property $\alpha_{n,i}=\alpha_{i,n}^{*}$ since $\Theta(ww^{\dagger})$ is a positive semidefinite matrix, (48) can be computed as

$$\bar{s}^{\dagger}\Theta(ww^{\dagger})\bar{s}=\alpha_{i,i}|\bar{s}_i|^2+\Re\left\{\sum_{\substack{n=1\\n\neq i}}^{KN_T}2\bar{s}_i\alpha_{i,n}s_n^{*}\right\}+\sum_{\substack{k=1\\k\neq i}}^{KN_T}\sum_{\substack{l=1\\l\neq i}}^{KN_T}s_l^{*}\alpha_{k,l}s_k. \tag{49}$$

Hence, we obtain

$$a_{0,i}=\alpha_{i,i},\ a_{1,i}=2\sum_{\substack{n=1\\n\neq i}}^{KN_T}\alpha_{i,n}s_n^{*},\ a_{2,i}=\sum_{\substack{k=1\\k\neq i}}^{KN_T}\sum_{\substack{l=1\\l\neq i}}^{KN_T}s_l^{*}\alpha_{k,l}s_k. \tag{50}$$

Following the same line of reasoning, the coefficients b_0, b_1, b_2 are given by,

$$b_{0,i}=\beta_{i,i},\ b_{1,i}=2\sum_{\substack{n=1\\n\neq i}}^{KN_T}\beta_{i,n}s_n^{*},\ b_{2,i}=\sum_{\substack{k=1\\k\neq i}}^{KN_T}\sum_{\substack{l=1\\l\neq i}}^{KN_T}s_l^{*}\beta_{k,l}s_k \tag{51}$$

where $\beta_{m,n}$ denotes the (m,n)th entry of $\overline{\Sigma}_{dv}(ww^{\dagger})$.

Author details

Guolong Cui*, Xianxiang Yu and Lingjiang Kong

*Address all correspondence to: cuiguolong@uestc.edu.cn

School of Electronic Engineering, University of Electronic Science and Technology of China, Chengdu, China

References

[1] Li J, Stoica P. MIMO Radar Signal Processing. Hoboken, NJ, USA: Wiley; 2009

[2] Haimovich AM, Blum RS, Cimini LJ. Mint:MIMO radar with widely separated antennas. IEEE Signal Processing Magazine. 2008;**25**:116-129. DOI: 10.1109/MSP.2007.909532

[3] Fishler E, Haimovich AM, Blum RS, Cimini LJ Jr, Chizhik D, Valenzuela RA. Spatial diversity in radars-models and detection performance. IEEE Transactions on Signal Processing. 2006;**54**:823-838. DOI: 10.1109/TSP.2005.862813

[4] Li J, Stoica P. MIMO radar with colocated antennas. IEEE Signal Processing Magazine. 2007;**24**:106-114. DOI: 10.1109/MSP.2007.904812

[5] Forsythe K, Bliss D, Fawcett G. Multiple-input multiple-output (MIMO) radar: Performance issues. In: Proceedings 38th Asilomar Conference Signals, Systems and Computers (ASILOMAR04); 7-10. Nov. 2004. Pacific Grove, CA, USA: IEEE; 2004. pp. 310-315

[6] Yang Y, Blum RS. Minimax robust MIMO radar waveform design. IEEE Journal of Selected Topics in Signal Processing. 2007;**1**:147-155. DOI: 10.1109/JSTSP.2007.897056

[7] Aubry A, De Maio A, Huang Y. MIMO radar Beampattern design via PSL/ISL optimization. IEEE Transactions on Signal Processing. 2016;**64**:3955-3967. DOI: 10.1109/TSP.2016.2543207

[8] Ahmed S, Alouini MS. MIMO-radar waveform covariance matrix for high SINR and low side-lobe levels. IEEE Transactions on Signal Processing. 2014;**62**:2056-2065. DOI: 10.1109/TSP.2014.2307282

[9] Friedlander B. Waveform design for MIMO radars. IEEE Transactions on Aerospace and Electronic Systems. 2007;**43**:1227-1238. DOI: 10.1109/TAES.2007.4383615

[10] Naghibi T, Behnia F. MIMO radar waveform design in the presence of clutter. IEEE Transactions on Aerospace and Electronic Systems. 2011;**47**:770-781. DOI: 10.1109/TAES.2011.5751224

[11] Chen CY, Vaidyanathan PP. MIMO radar waveform optimization with prior information of the extended target and clutter. IEEE Transactions on Signal Processing. 2009;**57**:3533-3544. DOI: 10.1109/TSP.2009.2021632

[12] Cui G, Li H, Rangaswamy M. MIMO radar waveform design with constant modulus and similarity constraints. IEEE Transactions on Signal Processing. 2014;**62**:343-353. DOI: 10.1109/TSP.2013.2288086

[13] Zhu W, Tang J. Robust design of transmit waveform and receive filter for colocated MIMO radar. IEEE Signal Processing Letters. 2015;**22**:2112-2116. DOI: 10.1109/LSP.2015.2461460

[14] Jiu B, Liu H, Wang X, Zhang L, Wang Y, Chen B. Knowledge-based spatial-temporal hierarchical MIMO radar waveform design method for target detection in heterogeneous clutter zone. IEEE Transactions on Signal Processing. 2015;**63**:543-554. DOI: 10.1109/TSP.2014.2366714

[15] Imani S, Ghorashi SA. Transmit signal and receive filter design in co-located MIMO radar using a transmit weighting matrix. IEEE Signal Processing Letters. 2015;**22**:1521-1524. DOI: 10.1109/LSP.2015.2411676

[16] Xue M, Zhu X, Li J, Vu D, Stoica PMIMO. Radar waveform design. In: De Maio A, Gini FL P, editors. Waveform Design and Diversity for Advanced Radar Systems. 2012. pp. 89-120. DOI: 10.1049/PBRA022.ch4

[17] Mecca VF, Krolik JL, Robey FC. Beamspace slow-time MIMO radar for multipath clutter mitigation. IEEE International Conference on Acoustics, Speech and Signal Processing 31 March-4 April 2008. Las Vegas, Nevada, USA: IEEE; 2008. p. 2313-2316

[18] Duly AJ, Krogmeier JV. Time-division beamforming for MIMO radar waveform design. IEEE Transactions on Aerospace and Electronic Systems. 2013;**49**:1210-1223. DOI: 10.1109/TAES.2013.6494408

[19] Karbasi SM, Aubry A, Carotenuto V, Naghsh MM, Bastan MH. Knowledge-based design of space-time transmit code and receive filter for a multiple-input-multiple-output radar in signal-dependent interference. IET Radar, Sonar, Navigation. 2015;**9**:1124-1135. DOI: 10.1049/iet-rsn.2014.0527

[20] Yu X, Cui G, Kong L, Carotenuto V. Space-time transmit code and receive filter Design for Colocated MIMO radar. IEEE radar conference; 2-6 May 2016; Philadelphia, Pennsylvania, USA. IEEE. 2016:1-6

[21] Cui G, Yu X, Carotenuto V, Kong L. Space-time transmit code and receive filter design for colocated MIMO radar. IEEE Transactions on Signal Processing. 2017;**65**:1116-1129. DOI: 10.1109/TSP.2016.2633242

[22] Guerci JR. Cognitive radar: The knowledge aided fully adaptive approach. IEEE radar conference; 10-14 May 2010; Washington, DC, USA. IEEE. 2010:1365-1370

[23] Aubry A, De Maio A, Farina A, Wicks M. Knowledge-aided (potentially cognitive) transmit signal and receive filter design in signal-dependent clutter. IEEE Transactions on Aerospace and Electronic Systems. 2013;**49**:93-117. DOI: 10.1109/TAES.2013.6404093

[24] Aubry A, De Maio A, Jiang B, Zhang S. Ambiguity function shaping for cognitive radar via complex quartic optimization. IEEE Transactions on Signal Processing. 2013;**61**:5603-5619. DOI: 10.1109/TSP.2013.2273885

[25] Cui G, Fu Y, Yu X, Li J. Local ambiguity function shaping via unimodular sequence design. IEEE Signal Processing Letters. 2017;**24**:977-981. DOI: 10.1109/LSP.2017.2700396

[26] De Maio A, De NS, Huang Y, Luo Z, Zhang S. Design of phase codes for radar performance optimization with a similarity constraint. IEEE Transactions on Signal Processing. 2009;**57**:610-621. DOI: 10.1109/TSP.2008.2008247

[27] Aubry A, Carotenuto V, De Maio A. Forcing multiple spectral compatibility constraints in radar waveforms. IEEE Signal Processing Letters. 2016;**23**:483-487. DOI: 10.1109/LSP.2016.2532739

[28] Aubry A, De Maio A, Piezzo M, Farina A, Wicks M. Cognitive design of the receive filter and transmitted phase code in reverberating environment. IET Radar, Sonar, Navigation. 2012;**6**:822-833. DOI: 10.1049/iet-rsn.2012.0029

[29] Cui G, Yu X, Foglia G, Huang Y, Li J. Quadratic optimization with similarity constraint for unimodular sequence synthesis. IEEE Transactions on Signal Processing. 2017;**65**:4756-4769. DOI: 10.1109/TSP.2017.2715010

[30] Yu X, Cui G, Ge P, Kong L. Constrained radar waveform design algorithm for spectral coexistence. IET Electronic Letters. 2017;**53**:558-560. DOI: 10.1049/el.2016.4524

[31] Li J, Guerci JR, Signal XL. Waveforms optimal-under-restriction design for active sensing. IEEE Signal Processing Letters. 2016;**13**:565-568. DOI: 10.1109/SAM.2006.1706159

[32] Barros AI, Frenk JBG, Schaible SA. New algorithm for generalized fractional programs. Mathematical Programming. 1996;**72**:147-175. DOI: 10.1109/CC.2017.7942327

[33] Crouzeix JP, Ferland JA, Schaible S. An algorithm for generalized fractional programs. Journal of Optimization Theory and Applications. 1985;**47**:35-49. DOI: 10.1109/IPDPS.2017.22

[34] Aubry A, De Maio A, Naghsh MM. Optimizing radar waveform and Doppler filter bank via generalized fractional programming. IEEE Journal of Selected Topics in Signal Processing. 2015;**9**:1387-1399. DOI: 10.1109/JSTSP.2015.2469259

[35] Golub G H and Loan C F V. Matrix Computations. 4th ed. Baltimore, MD: The Johns Hopkins University Press; 2013

[36] Grant M and Boyd S. CVX Package [Internet]. March 2017. Available from: http://www.cvxr.com/cvx.r

[37] Aubry A, De Maio A, Huang Y, Piezzo M, Farina A. A new radar waveform design algorithm with improved feasibility for spectral coexistence. IEEE Transactions on Aerospace and Electronic Systems. 2015;**52**:1029-1038. DOI: 10.1109/TAES.2014.140093